Hydrodynamic modeling of a complex salt marsh system: Importance of channel shoreline and bathymetric resolution

Key points:

- Poor grid resolution around marsh-channel berm creates artificial channel convergence and inaccurate tidal wave characteristics.
- Topo-bathymetry field survey and bias correction improves channel hypsometry and numerical model reliability significantly.
- Inaccurate channel bathymety and inadequate resolution might lead to acceptable surface elevation but poor tidal velocity field.
- The conventional grid generation methods based on sparse cross channel surveys is not sufficient for wetland models.

Hydrodynamic modeling of a complex salt marsh system: Importance of channel shoreline and bathymetric resolution

Mithun Deb[1], Ali Abdolali[3,4,5], James T. Kirby[2], Fengyan Shi[2]

1- Marine and Coastal Research Laboratory, Coastal Sciences Division, Pacific Northwest National Laboratory
2- Center for Applied Coastal Research, Department of Civil and Environmental Engineering, University of Delaware, Newark, DE 19716 USA
3- NWS/NCEP/Environmental Modeling Center, National Oceanic and Atmospheric Administration (NOAA), College Park MD USA
4- I.M. Systems Group, Inc. (IMSG), Rockville, MD 20852 USA.
5- University of Maryland, College Park, MD 20742 USA.

Abstract

Modeling hydrodynamics and sediment transport inside a multi-inlet wetland system is a challenging task due to constraints on model efficiency, accuracy and representation of physics, the scarcity of field data for model validation, and more importantly, the availability of high-resolution data sets of channel bathymetry. Lack of field data sets, model assumptions, and limitations often lead to wrong interpretation of the systems nature. To correctly predict the changes in governing hydrodynamics and morphology of shallow wetland environments, it is essential to resolve the channel properties with the best possible accuracy. In this study, we consider the importance of two factors, numerical model grid resolution around channel shorelines, and bathymetry surveys, in improving the interior channel and mudflat hydrodynamics. Channel shoreline element size is observed to be an essential factor in time-varying channel volume estimation. Lower model resolution in channels inside a marsh can provide good agreement with in-situ surface elevation data, even though the channel surface-velocity phase lag, and velocity magnitude and asymmetry are inaccurate. A higher grid resolution at the channel berms and the high-density channel survey help define the time-varying lateral shoaling bathymetry, cross-section area, and bottom friction, and improve the corresponding model skill and tidal wave properties significantly. We have selected Bombay Hook National Wildlife Refuge, a rapidly eroding salt-marsh system in Delaware Bay,

to compare model skills for different hypsometric conditions. Model performance is evaluated during two storm conditions; Hurricane Sandy (2012) and Hurricane Joaquin (2015), using tide gauges located on the marsh interior channels.

---

1. Introduction

The stability and long-term sediment transport in a tidal wetland system largely depend on the channel flow characteristics and morphology. Sediment transport directly correlates with the surface elevation/velocity asymmetry, that can be in the form of magnitude and period of the tidal wave (Friedrichs and Aubrey, 1988; Nidzieko, 2010; Ralston et al., 2012). Having an accurate estimate of tidal asymmetry and relative phase difference between current and surface are essential for determining residual flow, direction and sediment budget. In a channelized wetland system, tidal distortion (duration asymmetry and/or velocity skewness) varies when wave travels from inlet mouth to the boundary due to interaction between non-linear terms in the continuity and momentum equations (Parker, 1984; Aubrey and Speer, 1985; Friedrichs and Aubrey, 1988). More specifically, the space and time varying channel cross-section area, advective acceleration and quadratic friction play a major role in the generation of overtides and higher harmonics. In an estuarine system with negligible river discharge, besides asymmetry, the relative phase difference between tidal velocity u and surface elevation η can also vary both spatially and temporally due to system geometry, bottom friction and inter-tidal storage volume (Boon and Byrne, 1981; Friedrichs and Aubrey, 1988). The phase difference $\phi_{\eta u}$ between surface elevation and velocity has historically been used to characterize the tidal oscillations in an estuary as standing waves, progressive waves, or a combination of both (Parker, 1984; Jay, 1991; Friedrichs, 2010). For the finite channels, wave properties can change in the presence of strong bottom friction, where the incident and reflected wave amplitudes decay and their phase lag follows the friction force (Hunt, 1964). Beside channel bottom friction, the channel hypsometry change based on the tidal surface elevation can also affect the amplitude decay and phase lag by enhancing or reducing the topographic dissipation (Li and Hodges, 2020). To properly identify the tidal wave characteristics and flow asymmetry inside a wetland

system, we need a robust numerical modeling system that can resolve the variation in channel-marsh shoreline boundary and hypsometry with higher accuracy.

1.1. Background on modeling limitations in a marsh-channel system

1.1.1. Model grid resolution and the wetland flooding and draining

All of the studies mentioned above have evaluated dominant physical processes for $\phi_{\eta u}$ phase increase/decrease in channelized estuaries using simplified 1D wave or diffusion equations. These models have some common assumptions when dealing with the channel geometry, such as exponential channel width increase or decrease, depth is cross-section averaged, or the channel has a prismatic shape (Friedrichs, 2010). In a complex wetland system, to predict smaller scale processes, the along and across-channel bathymetry variations are key factors in determining time and space varying amplitude-velocity phase difference that a 1D model is not capable to resolve. To take care of the lateral and vertical channel variations, a 2D model is required with enough resolution to resolve the tidally varying hypsometry. However, developing an efficient high fidelity wetland/salt-marsh 2D model is a challenging task as it requires an understanding of the optimum grid resolution and more importantly availability of high resolution data sets of marsh topography and channel bathymetry (Temmerman et al., 2005, 2012). Each of them has limitations such as spatially variable biases due to the presence of vegetation and temporal variations due to seasonal or severe events changes. Until now, a large number of studies have been done to address estuarine/coastal circulation problems using structured curvilinear (Lesser et al., 2004; Chen et al., 2014), unstructured/triangular (Luettich Jr et al., 1992; Chen et al., 2008) and hybrid grids (Bomers et al., 2019) in finite difference, finite element or finite volume discretization frameworks. In complex wetlands where bathymetry and/or topography gradient is large, an unstructured grid offers better performance in terms of shape flexibility and computational efficiency (Dietrich et al., 2012; Symonds et al., 2017). Inside a wetland system, the model performance then depends on changes to unstructured grid resolution following the variation of topo-bathy gradient, which can affect marsh-channel draining and filling. In inter-tidal zones like wetlands, it is essential to have a highly accurate land-water interface line for estimating the volume of water that goes back and forth

between channel and marsh surfaces. It affects the time-varying channel hypsometry, which then alters the channel flow continuity and momentum. For these reasons, it is mandatory to correctly resolve the land-water flow exchange and channel hypsometry with the most satisfactory grid resolution possible to have an accurate estimation of tidal amplitude, phase speed, and asymmetry inside a wetland system.

With that being said, addressing all the smaller-scale bathymetric features in the model calculation can be expensive due to significant computational time and memory storage. Defina (2000) proposed a subgrid model to speed up the computational efficiency while taking care of the higher-resolution topographic data. An artificial porosity parameter is estimated using the ground unevenness within coarse grid cells and incorporated into the governing equations to improve volumetric flow rates in/out of the cells with much less computational effort. Several studies such as Sanders et al. (2008), Volp et al. (2013), and Wu et al. (2016) have modified and enhanced the subgridding technique for different urban flood and tidal hydrodynamic modeling applications in the last two decades. However, despite the recent progress in subgrid methods, getting the coarse grid model to reflect the actual channel conveyance, surface area, and water volume is still challenging and can be time and labor-consuming (Li and Hodges, 2020). Especially in a complex wetland system with a sharp marsh-channel edge and rapid bathymetry change, we need to carefully represent the small-scale features to resolve the shifts in wetting and drying fronts and topographic dissipation.

1.1.2. Channel bathymetry data

Although a grid with enough resolution for resolving all the major processes is an important need, the model performance can be constrained by the scarcity of unbiased marsh topography and channel bathymetry data (Yu and Lane, 2006; Horritt et al., 2006). Recently, the emergence of different remote sensing techniques such as Light Detection and Ranging (LiDAR; e.g., Horritt et al. (2006)) and Interferometric Synthetic Aperture Radar (SAR; e.g., Horritt and Bates (2001)) have significantly improved the overland flood modeling, where the spatial resolution can reach up to 1 m with a vertical accuracy of ±15 cm on bare ground (Yu and Lane, 2006). However, these data sets have some major drawbacks that includes inability to map the chan-

nel bathymetry, only limited to dry areas and can have vegetation bias based on the data acquisition period (tidal stage and seasonality). While the vegetation bias in the LiDAR data can be treated via a number of techniques such as minimum bin technique (Schmid et al., 2011), the proper representation of channel bathymetry is still a challenging task. To make seamless topo-bathymetric DEMs in wetlands, that include shallow turbid water bodies, the most popular and reliable technique is the use of an acoustic sonar system that can map the seafloor from single or multi-beam echo sounding (Dierssen and Theberge, 2014). Inside a coastal wetland system that has major channels and tidal mudflats, it is imperative to collect high density bathymetry data to properly represent the channel hypsometry in model calculations.

1.2. Present study

This study assesses the role of grid resolution and accuracy of topobathymetric data on the tidal wave propagation and velocity asymmetry, to determine the role of inaccurate representation of the major channels hypsometry in reducing model reliability inside the wetland. The case study is Bombay Hook National Wildlife Refuge (BHNWR), DE located on the western shore of Delaware Bay, which as one of the largest multi-inlet tidal wetland system in the mid-Atlantic region, is rapidly eroding salt marsh system with short length ($\sim 16km$), non-convergent and deep channels ($\sim 10m$ from NAVD88) (Figure 1a). The system has two major inlets, namely Sluice Ditch and Leipsic River, that are responsible for two-thirds of the total volume transport (Deb et al., 2022a). Other important information about the study areas geographic coverage, economic significance and ongoing wetland loss is detailed in Deb et al. (2022a). In this study, the 2D model performance is described after implementing a sufficient grid resolution that resolves marsh-channel interface properly and a dense channel survey data, which in fact provides a more realistic estimate of the tidal regime and velocity asymmetry.

This paper is organized as follows. Sections 2.1.1 and 2.1.2 describes unstructured grid development, the pre-exisiting grid-A from a previous study and new ones (B,C) using bias corrected high-resolution LiDAR data set with surveyed marsh elevation for topography and channel data for bathymetry. Section 2.2 provides a brief overview

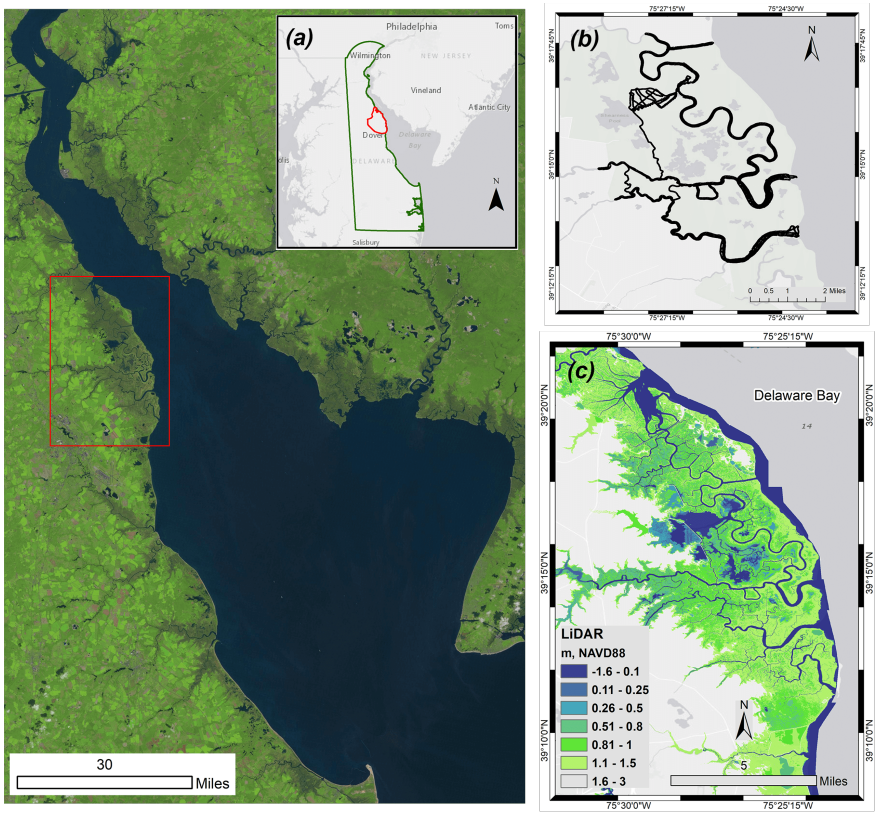

Figure 1: (a) Top: The state of Delaware, U.S., Bottom: USGS Landsat imagery for the Delaware Bay (`https://glovis.usgs.gov/`), the red polygons show the study area, Bombay Hook National Wildlife Refuge, DE (b) channel survey track lines inside the wetland (c) NOAA 2011 LiDAR data set of marsh surface (in meters, vertical datum: NAVD88)

of the hydrodynamic model physics and closures for the depth-integrated 2D version. Model results for stormy conditions are given in Section 3, illustrating model inconsistency that emerges from changes to the grid resolution and topobathymetry. A detailed description of the significant modeling bias from inaccurate channel hypsometry, and how a proper channel survey data can improve overall tidal hydrodynamics and model accuracy are given in section 4. Concluding remarks and observations on the necessity of the future works are discussed in section 5.

2. Methods

2.1. Model grid development

In this section, we describe the development of different DEMs, and how they have been used for computational grid generation and terrain representation.

2.1.1. Topo-bathymetric DEM

For the study area BHNWR, three high resolution LiDAR data sets of the years 2007, 2011 and 2014 are collected from different sources (Deb et al., 2018a), processed to a regular grid with 1 m resolution and referenced to the NAVD88 datum. These data sets are compared with the ground truth survey at different locations to identify the most reliable one with minimum vegetation bias. Metadata, accuracy and extent of these data sets are described in Deb et al. (2018a). The National Oceanic and Atmospheric Administration (NOAA) 2011 data set has the least bias compared to other data sets and therefore was used for the high-resolution model development of BHNWR (Figure 1c). In this study, two sets of 2011 LiDAR data are used, where one represents actual NOAA post-processed data that contains vegetation bias; previously used in a similar hydrodynamic study by Stammerman (2013), and a modified one that has been corrected using ground truth, field vegetation survey and vegetation maps.

For the bathymetry, NOAA-NGDC data sets were collected for the bay side of the domain, developed from depth soundings for the Delaware Bay and Estuary (Stammerman, 2013). The NOAA-NGDC data does not have a good representation of the channels inside BHNWR system and required a separate field survey of the major channels and tidal creeks. In a previous study of the same area, Stammerman (2013) measured a total of 48 cross sectional profiles on the major channels and 5 on the mudflats using hand-held sonar, and used linear interpolation of the bathymetry along channels in between the cross sections. The surveyed data points were referenced vertically to NAVD88 datum and interpolated to model NOAA-NGDC DEM for final model bathymetry of the area. For a large wetland like BHNWR, this channel survey data is not sufficient to properly represent along-channel cross sectional geometries. For the present study, a bathymetric survey of the main waterways in BHNWR was conducted

using single-beam echosounder to obtain continuous depth with much higher density (Deb et al., 2018b). The survey consists measurement of depth and horizontal coordinates along cross sections, middle and sides of the channel profile and multiple zig-zag patterns (Figure 1b). The raw bathymetric soundings were processed, detided using nearest tide gauges, evaluated for outliers and then referenced to horizontal and vertical datums: Universal Transverse Mercator (UTM) Zone 18 and NAVD88 respectively. Additional information on the survey and pre/post processing of the data set is given in Deb et al. (2018b). The new channel bathymetry information then interpolated back to the previously developed data set of Stammerman (2013), and channel representation from both low and higher density survey data sets are shown in Figure 2.

Finally, from the collected and surveyed marsh topography and channel bathymetry data sets, we made two different seamless topo-bathymetric DEMs for this study using: 1) NOAA 2011 LiDAR data set and sparse channel survey done by Stammerman (2013), and 2) Bias corrected NOAA 2011 LiDAR and new dense channel survey data of the entire BHNWR.

2.1.2. Unstructured grid

Two unstructured grids of varying element sizes are generated, with identical nodes coordinates inside the bay and different resolutions inside the wetland system to describe how a small change in grid resolution can significantly affect the overall tidal regime, and provide an ambiguous modeling solution.

An unstructured grid covering the entire wetland with sufficient resolution for resolving tidal processes, was available from a previous hydrodynamic study of BHNWR (Stammerman, 2013). The model grid domain covers interior Delaware Bay from Bowers, Delaware on southern boundary up to 39° 25′ N latitude on Delaware River, and has a total of 370629 nodes and 740776 elements. Stammerman (2013) used a mesh generation tool JANET (`http://www.smileconsult.de/index.php`) that applies forcing polygons or break lines to enforce the alignment of elements along the marsh-channel shoreline. The nodes on the forcing polygon were distributed manually based on the desired distance in specific areas, and the basic triangulation connected these nodes. The nodes on the tidal channels were pre-defined, and the mesh resolution

transitioned from small elements in channels to bigger elements over the marsh surfaces, neglecting the steep channel side walls and berms (Figure 3a.1). In a tidally varying environment, the unresolved channel berms can change the land-water interface and channel width dramatically, causing artificial channel convergence/divergence following low/high tide. To tackle this problem, the resolution of the existing grid of Stammerman (2013) was increased, mostly in the major channels, tidal creeks and land-water interface covering elevated berms (Figure 3a.2, b.2). The zero NAVD88 elevation contour is used to define the channel lateral boundaries, and the bathymetry gradient is then used to increase the resolution in channel areas with higher gradients. As a result, the interior channels, berms and channel shorelines have higher resolution compared to the marsh platform. The new grid has an element size as fine as $\sim$ 3 m around marsh-channel boundaries, and in total has 488207 nodes and 975931 elements. Ultimately, using these two different resolutions and two channel bathymetry data sets, three unstructured grids are used for the analysis (Figure 3). We used a linear interpolation scheme that generates triangular irregular networks (TIN) and piecewise linear surfaces from scattered points to interpolate the topo-bathymetry into the model grid (Aquaveo, 2016). The grids are unique in representing channel hypsometry based on the tidal elevation, where the main properties are:

1. Grid-A: lower channel resolution and insufficient channel survey, collected from Stammerman (2013) (Figure 2a, top subplot and 3b.1)
2. Grid-B: higher channel and berm resolution, and bathymetry from Stammerman (2013) (Figure 2a, top subplot and 3b.2)
3. Grid-C: higher channel and berm resolution, new dense channel survey data set (Figure 2a, bottom subplot and 3b.2).

The dramatic difference between sparse and dense bathymetric survey data set is shown in Figure 2a,b. In Figure 2b, we can see that there is a significant difference between cross section averaged depths estimated from different grids along the Leipsic River, which could bring errors to the overall model performance and tidal hydrodynamics.

2.2. Modeling background and boundary forcings

For this study, we use the Finite-Volume, primitive equation Community Ocean Model (FVCOM) developed by Chen et al. (2008), which is an unstructured grid model and widely used for resolving coastal scale processes both in 2D and 3D. The 2D model is driven with two different sets of boundary conditions: 1) Water level and depth average velocity fields from the large scale three-dimensional model of Delaware Bay: Coupled-Ocean-Atmosphere-Wave-Sediment Transport (COAWST) (Kukulka et al., 2017) directly nested at the unstructured grid open boundary nodes for stormy conditions and 2) local M_2 tidal amplitude and period at open boundaries to reproduce a calm condition without channel berm overtopping. While the first set of simulations will show the role of grid resolution and quality of topobathymetric data in model under/over-prediction and phase lag during Hurricane Sandy and Hurricane Joaquin, the second set will explain qualitatively how a significant portion of the phase lag can be generated solely from the inaccurate channel bathymetry, and influence the overall tidal regime and velocity asymmetry.

Both meteorological events Hurricane Sandy (2012) and Hurricane Joaquin (2015) used for model vs. in-situ comparison had threatened the Delaware Bay with storm surge and large-scale coastal flooding (Dohner et al., 2016). Hurricane Sandy made landfall on the New Jersey coast near Brigantine, NJ (Sullivan and Uccellini, 2013), and Hurricane Joaquin initially made landfall in the Bahamas and then changed track, finally moving north-northeastward over the Atlantic Ocean. Hurricane Joaquin stayed away from the US mainland and close to the shelf; however, significantly affected the the DE and Chesapeake bay area because of its gradually amplified surge generated for a longer period compared to Hurricane Sandy. COAWST large scale simulations for the entire Bay included the necessary forcings such as atmospheric forcing, tidal constituents and river discharge data from multiple sources, and were validated against NOAA tide gauges located in the Bay (Deb et al., 2022a). Then, after nesting COAWST data at the FVCOM boundary, four tide gauge data sets, located on wetland interior channels (Figure 3a.2) are used to evaluate the model performance for different prescribed grid conditions. The tide gauges have information from the year 2008 to 2019 and regularly maintained by the Delaware Department of Natural Resources and

Environmental Control (DNREC). After collection, all data sets were post-processed and converted to water surface elevation referenced to the NAVD88 datum. Among the channel tide gauges, "Navigation light" is located on the major channel/inlet mouth, "Dock" is close to the model upstream boundary, and two other gauges "Leatherberry" and "Shearness" are from inside the wetland and near a tidal mudflat, as shown in Figure 3a.2. For this study, a small portion of the entire channel tide gauge data is taken for model comparison representing the major storm events: Hurricane Sandy and Hurricane Joaquin.

More information about 2D model code, methods for prescribing tidal and subtidal boundary condition, validation and its limitations are given in Deb et al. (2022a). For the second part of the study, to simulate channel flooding and draining without marsh overtopping, the principal lunar semi-diurnal constituent M_2 amplitude and period are extracted from the nearest Bay tide gauge Ship John Shoal, NJ (`https://tidesandcurrents.noaa.gov/`) using T_TIDE, a tidal harmonic analysis tool (Pawlowicz et al., 2002). For different model runs, all the physical parameters such as drag coefficient, mixing coefficient and others are kept the same as cases in Deb et al. (2022a). Finally, we ran all the cases in a distributed-memory, Linux cluster using Intel Ivy Bridge 120 processors per case.

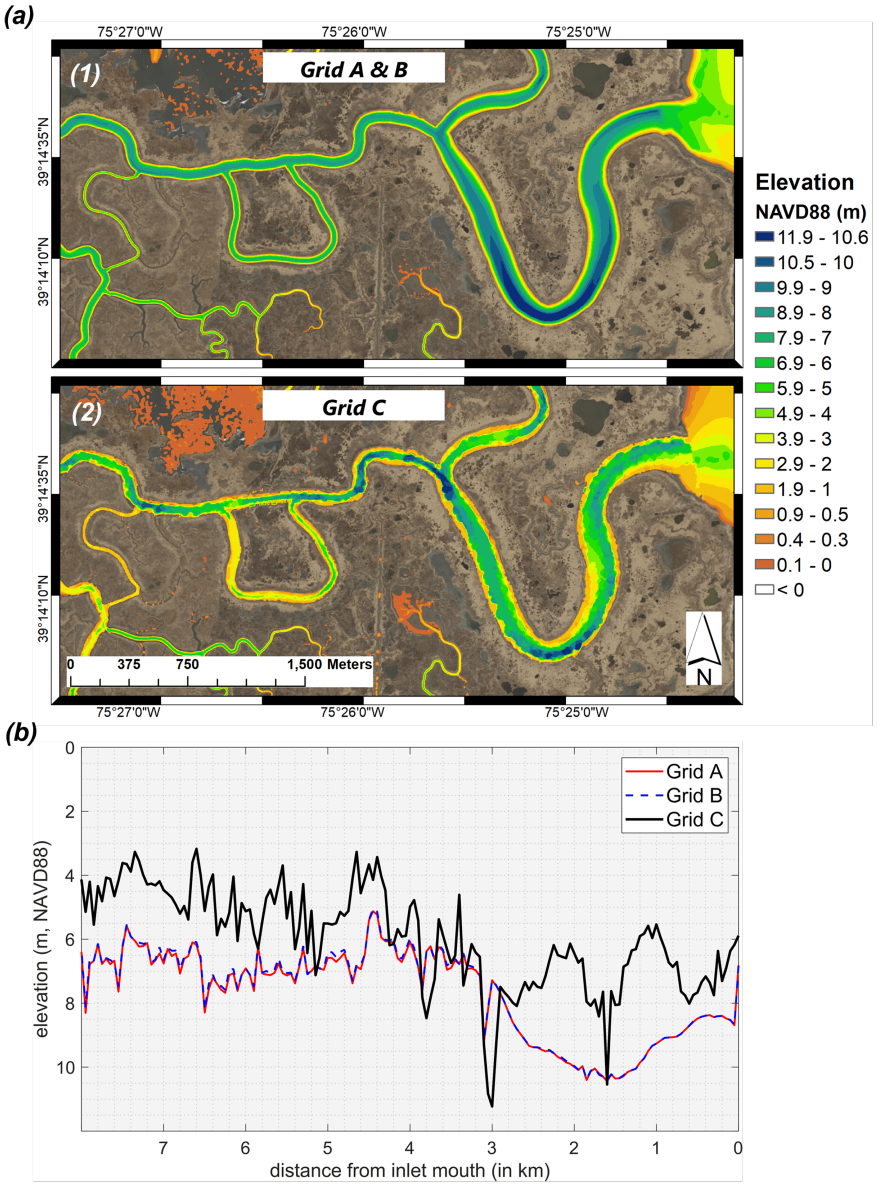

Figure 2: Bathymetry in a major channel: Leipsic River from different survey data sets interpolated to the model grids; (a) spatial variation of channel elevation from NAVD88 datum (in meters): top subplot represents interpolation from low density channel survey, and bottom subplot is from the high density survey conducted during the study; (b) cross-section averaged bathymetry from inlet mouth to boundary (in meters)

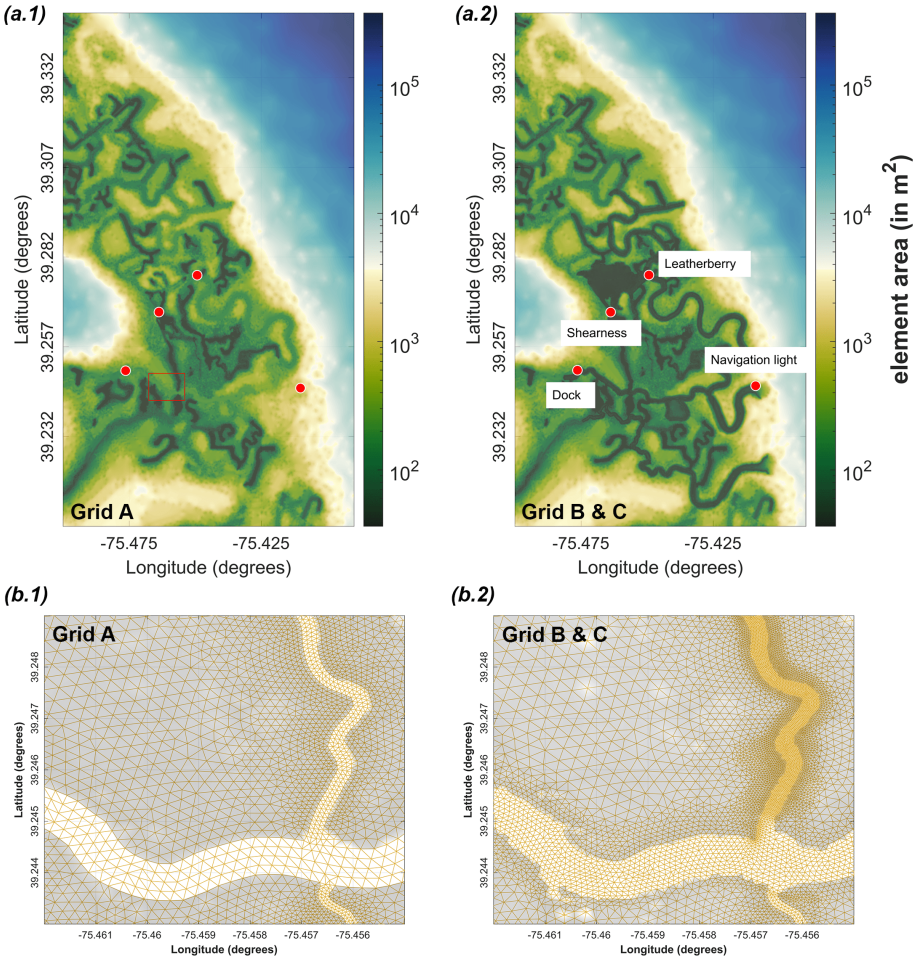

Figure 3: (a) Unstructured grids with different resolutions, separated into two columns showing: (a.1) low resolution in channels and on berms (a.2) high resolution in channels and on berms. Red circles show channel tide gauges used for the model validation; (b) Similar comparison as (a) for a small portion of the wetland shown using the red polygon in subplot a.1.

3. Results

In this section, water surface elevations from model and in-situ data during the storm events are compared in Figure 4-7 to understand the role of proper channel resolution and hypsometry on accurate wetland flood modeling. The comparisons have been assessed in terms of model skill (Willmott, 1981) and average bias index (Equation 1-2), where a model skill of 1.0 shows perfect agreement and a positive/negative bias represents model over/under-prediction respectively.

$$Bias = \frac{\sum_{n=1}^{N}(M_n - O_n)}{\sum_{n=1}^{N} O_n} \tag{1}$$

$$Skill = 1 - \frac{\sum_{n=1}^{N}(M_n - O_n)^2}{\sum_{n=1}^{N}(|M_n - O| + |O_n - O|)^2} \tag{2}$$

Where N is the total number of samples, M_n is the model result, O_n is the observed data and O is the mean of the observed data.

Here, more emphasis is given to the cases with Hurricane Joaquin (2015) where more field deployments, including current profiler data, are available. Figures 4-7 shows surface elevation comparison and statistics at channel tide gauges during Hurricane Joaquin and Hurricane Sandy, and both Figure 4 and Figure 6 are separated into two sub-figures: (a) showing the difference before the arrival of main surge and (b) during major event when the entire wetland system was submerged. Main comparison drawn here is between the in-situ and model results from three different grid configurations (A, B & C), described in the previous section. The differences between model results from Grids A - B and Grids B - C are due to grid resolution and accuracy of topobathymetric data sets respectively.

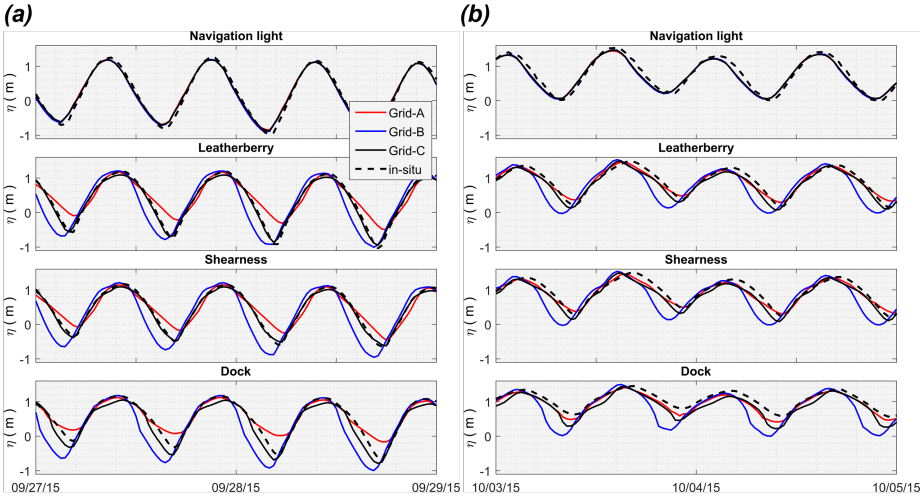

Figure 4: Water surface elevation from FVCOM model grids (straight lines) and in-situ (dashed line) during Hurricane Joaquin, 2015 at different channel tide gauge locations (in meters, from NAVD88 vertical reference level) (a) before the main surge event (b) during surge event.

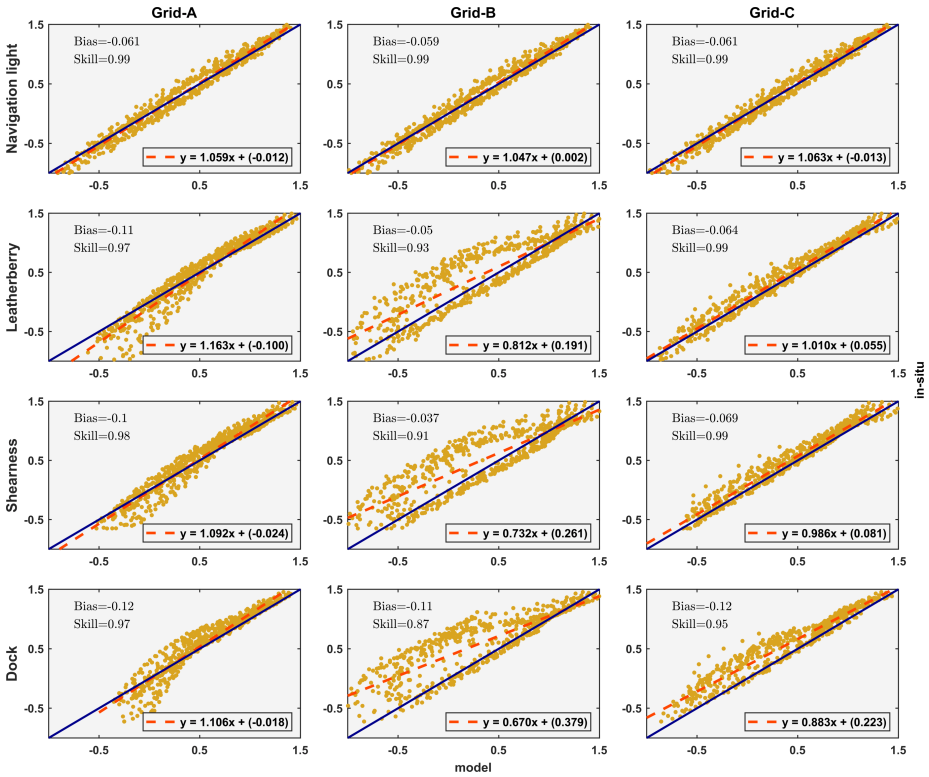

Figure 5: Scatter comparison: average bias index and skill between FVCOM model grids (separated into 3 columns) and in-situ water surface elevation at different channel tide gauge locations during the entire model period of Hurricane Joaquin, 2015 (in meters, from NAVD88 vertical reference level).

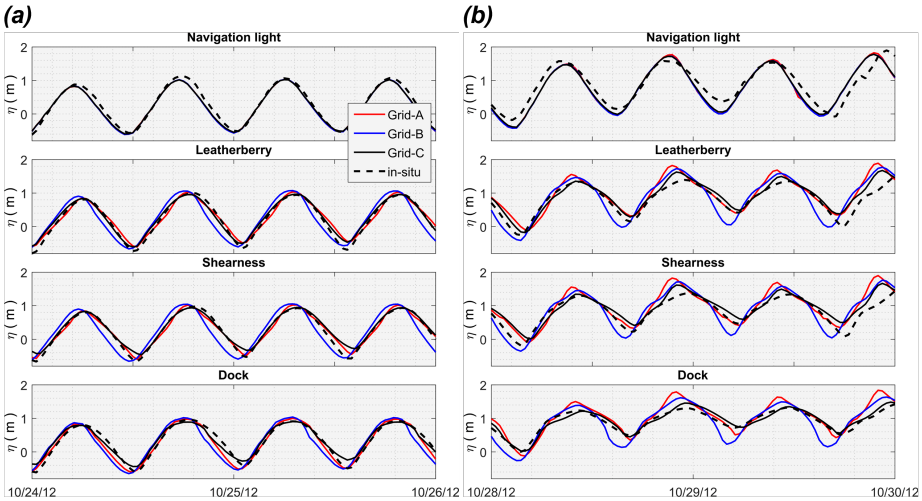

Figure 6: Water surface elevation from FVCOM model grids (straight lines) and in-situ (dashed line) during Hurricane Sandy, 2012 at different channel tide gauge locations (in meters, from NAVD88 vertical reference level) (a) before the main surge event (b) during surge event.

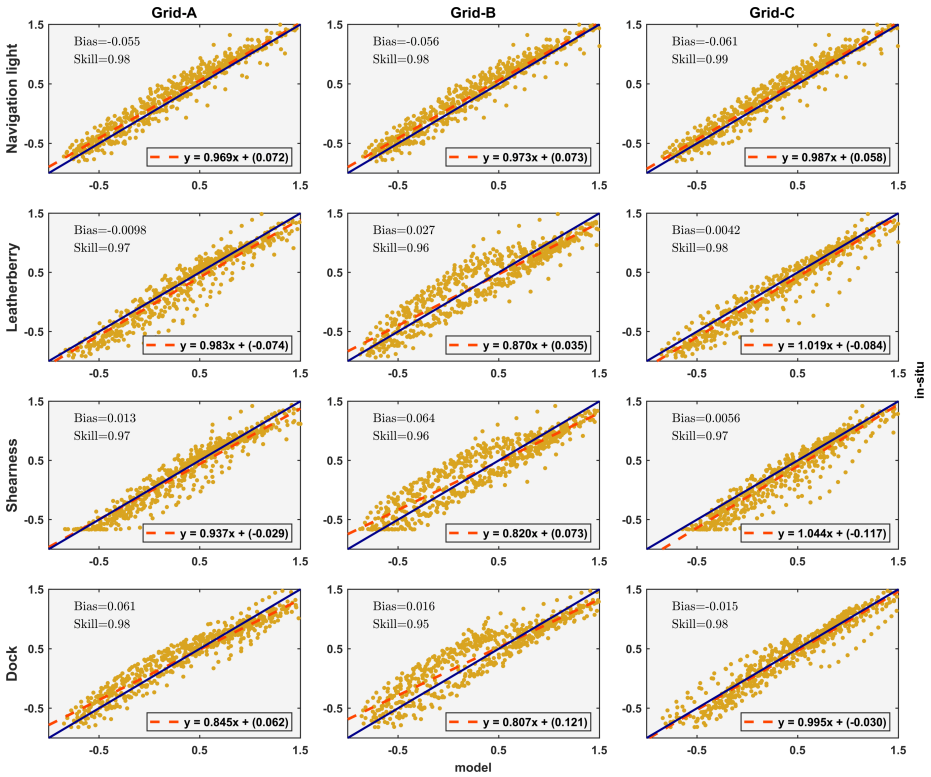

Figure 7: Scatter comparison: average bias index and skill between FVCOM model grids (separated into 3 columns) and in-situ water surface elevation at different channel tide gauge locations during Hurricane Sandy, 2012 (in meters, from NAVD88 vertical reference level)

We first examine the Grid-A case, which has a lower resolution in the channels and sparse bathymetry data. With this grid and a 2D mode explicit time-step of 0.15 s, we needed on average 2.6 hours to simulate one day. For Hurricane Joaquin (Figures 4-5), model performance is relatively better close to the inlet opening (Navigation light) than the interior gauges. Overall, model skill remains close to 0.97, which indicates that Grid-A is a reliable option for further model analysis. However, before the entire marsh submergence during Hurricane Joaquin, there is a higher bias that originated from model under-prediction of surface elevation during low tide, and the reduced tidal range along the channel as tide propagates inward from Navigation light to Dock (Figure 4). Then, when the major surge event inundates the marsh platform (Figure 4b), a better reproduction of channel flooding and draining is observed, and subsequently higher skill at all the gauges is achieved. These differences display the role of marsh surface flooding and draining in overall model performance, where before the major surge, we have an active model wet/dry domain in contrast to the complete wet domain during the marsh submergence. Interestingly, the same grid shows a better skill during calm conditions before Hurricane Sandy residual surge, and channel draining also seems to be accurate compared to the case of Hurricane Joaquin (Figures 6 and 7).

Grid-B has an increased resolution in order to resolve the land-water interface during tidal fluctuations better; however, the channel bathymetry is interpolated from the DEM used to construct Grid-A. For this case, with a similar time-step of 0.15 s, the model took on average 3.1 hours to simulate one day, a 19% increase from the previous setup. For the case of Grid-B, a drastic change in the scatter comparison is observed for both storm conditions, much more pronounced during Hurricane Joaquin. The model skill deteriorated faster inside the wetland (Figure 5, middle column), and the trend is significantly different from Grid-A. The time series plot during a calm condition is shown in Figure 4, when the system still has active wetting/drying, to understand this reduction in model skill. It shows improvements in channel draining and tidal range prediction during low tide conditions. The previous trend of under-prediction at the interior channel gauges has changed to over-prediction with a significant increase in phase mismatches. These low tide over-prediction and sharper drops to the trough compared to in-situ ultimately deteriorated the model skill. The phase lag remains

during the elevated MWL when wet part of the domain expands (Figure 4b), slightly less pronounced during Hurricane Sandy (Figure 6-7). This case with Grid-B raises a new concern that with an improved marsh-channel resolution, why does the system now show a higher phase lag during ebb and if it is solely from the inaccurate surveyed channel bathymetry. A detailed explanation of the tidal phase speed discrepancy due to inaccurate channel bathymetry is given in the discussion section.

For Grid-C, with Grid-B resolution and more accurate topobathymetry, an immediate improvement in wave phase prediction, tidal range, and channel draining/flooding is observed (Figure 5b, last column). Scatter comparison in Figure 4 show that the model skill and slope are close to 1.0 during the full period of Hurricane Joaquin, and also a similar response during Hurricane Sandy (Figure 6 and 7). Note that the slightly inaccurate sub-tidal forcing at the boundary, originally came from the large scale model and led to inaccurate sub-tidal signals in the entire domain, including the bayside gauges (Deb et al., 2022a). Finally, results using Grid-C show the importance of along and across channel bathymetry in resolving the hydrodynamics and tidal processes with higher accuracy.

4. Discussion

In the results section, we have shown surface elevation comparison at different channel locations inside BHNWR wetland system during Hurricane Joaquin and Sandy for different grids, and how the model responds to the changes in channel hypsometry (Figures 4-5, 6-7). We can see that the agreement between model and in-situ elevation varies based on different grid configurations. Our study area BHNWR can be considered a short estuary system. The wetland basin length is close to 20 km and is much shorter than the tidal wavelength of 400 km for a semi-diurnal tidal period of 12.42 hours (Parker, 1984). Channels are mostly narrow (~200 m), weakly-converging and deep at the middle (~10 m); however, the cross-sectional area varies significantly over the entire reach due to shallow/deep side banks. In-situ tide gauge data sets have shown that the tidal amplitude decay rate is insignificant, while there is a noticeable lag in phase when the wave travels upstream (Figure 8b). In the results section, we have observed that the model performs well at the gauge location close to the open bay (Navigation light) for all grids and storm events. However, when we looked into the marsh interior, the model predicts the surface better during rising tide compared to the falling. We explain the changes in model performance and tidal characteristics from different grid resolution and topobathymetry conditions in the following sections.

4.1. Role of marsh-channel connectivity and artificial ponding on model performance

Mainly, in Grid-A which has a lower resolution in channels, we can see that it under-predicts surface elevation during low tide, but then Grid-B with higher resolution over-predicts surface and misses phase completely (Figure 4-7). Subsequently, model prediction improves immediately during both high and low tide when surveyed channel bathymetry interpolated into Grid-B, represented as Grid-C. In Grid-A with previously collected bathymetry and lower resolution, the model suffers from inefficient marsh interior channel connectivity, along with a process called artificial ponding over the marsh platform (a modeling limitation from LiDAR and model grid resolution), ultimately leading to inaccurate drainage during low tide. Artificial ponding comes from the unresolved small marsh channels/creeks in the model grid that, in reality, drains the

isolated low spots in DEM depressions formed by channel berms. A detailed description of the ponding problem and the ongoing work is provided in Deb et al. (2018a). For this paper's scope, the importance of artificial ponding is less significant than the grid resolution in marsh-channel berm locations and the need for proper channel survey data.

During Hurricane Joaquin, the volume of water stored over the marsh surface was significant due to a longer surge period. The land-water interface along the channels was not resolved properly in the low-resolution grid, and it took a longer time to drain the stored water properly. As a result, the ebb duration increased, and the rising tide caught falling tide before reaching it's lowest limit in the channels. With improved resolution and properly defined channel berms in Grid-B, we observed an immediate improvement in the internal channel drainage pattern. The well-resolved channel berms had helped separate channels from marsh surfaces when the water level dropped below the model minimum depth of 5 cm. The surface elevation reaches close to in-situ elevation during low tide in the channels; however, it drains water faster than previous, causing a phase lag between model and in-situ. An increase in resolution, while keeping old bathymetry in place have raised the channel volume flux and shifted it toward a frictionless estuary, explained further in the following section. Then, with new survey data in Grid-C, we found that the middle and cross-section averaged channel bottom is much rougher compared to previous conditions (Figure 2) and it improves the representation of shallower zones close to channel banks. The channel survey data has also changed the spatially varying friction and helped predict the phase better, as shown in Figure 4-5. The response is also similar for Hurricane Sandy shown in Figure 6-7.

4.2. Channel hypsometry and surface phase lag

From Figure 6.a we can see that, Grid-B has surface elevation phase lag at wetland interior gauges (Leipsic, Shearness & Dock), even when there was no subtidal elevation and ponding right before Hurricane Sandy. Grid-A developed with low-resolution channel representation shows a good surface elevation agreement with in-situ at the same interior gauges. In this section, we explain this phase lag without any artificial storage over marshes, and also describe how an inaccurate representation of channel

configuration from collected data or model grid resolution can provide ambiguous results that are in good agreement with the in-situ data. We ran new cases with only a regular M_2 tide that has an amplitude of 0.8 m and a period of 12.42 hr, keeping the grid properties unchanged. In Figure 8, we have surface elevation comparison between at the two tide gauge locations along the main tidal channel Leipsic River: Navigation light (at the inlet mouth) and Dock (close to the boundary, 9 km upstream).

First, we have compared model surface elevation for Grid-A and observe that there is a clear phase lag between the gauges during both rising and falling conditions (Figure 8a). When improved the resolution in channels and marsh surface for Grid-B, phase lag goes away, and the solution represents a standing wave condition. Ultimately, with the surveyed channel bathymetry in Grid-C, we see a reestablishment of the phase lag between downstream and upstream gauges, but much more pronounced during falling tide. The low-resolution grid elements in Grid-A that represent channel-marsh boundary cause connectivity issues during low tide due to minimum depth criteria defined for wetting/drying. As surface drops below minimum depth, nodes that are located over marsh edge makes the entire element fall into a dry category, ultimately making the channel width narrow than the original configuration shown in Figure 9a and 10a. Figure 10a (mid-column) shows a transect taken from mid-reach of the Leipsic River, where we can see that the width of the momentum transporting channel becomes almost half for most of the tidal cycle that slows down the wave propagation during both flood and ebb. With the higher resolution in channels and berm location, we overcame the abrupt channel width contraction and expansion issue in Grid-B. Although, it changed the channel hypsometry from previous, the interpolated bathymetry remains inaccurate (Figure 2). From Figure 9b and 10b, we can see a much smoother transition between marsh and channel during high and low tides. In all of our previous surface elevation comparisons between model and in-situ shown in the results section, we have the largest bias for Grid-B than the other grids. In Figure 8a (second subplot) we can see that there are no changes in surface elevation phase, $\phi_{\eta\eta}$ for the entire channel reach and wave phase speed is a constant ($c = \sqrt{gh}$) at both flood and ebb, mimicking a frictionless, non-convergent estuary with a barrier at the head (Van Rijn et al., 2010). Ultimately, using Grid-C with surveyed bathymetry and a proper representation of the

channel geometry, we noticed an increase in surface elevation phase lag again at both inlet mouth and boundary, much more pronounced during ebb condition (Figure 8a (bottom subplot)). From Figure 9c and 10c, we can see that the width becomes almost similar to Grid-B during a high tide, while the well-defined shoals close to channel banks reduced cross-section averaged depth significantly. Lateral channel depth varies throughout the entire reach, and represents a channel geometry with a deep channel at the middle and shallow side banks. In Figure 8a (bottom subplot), we can see that the flood tide propagates faster corresponding to the narrower and deeper channel section at the mid-channel and slows down during ebb due to the reduced depth. To compare the model phase estimates with the in-situ data, we have selected a neap tide condition with minimum marsh flooding, and provided a comparison between in Figure 8b. Figure 8b shows a similar phase difference as observed using Grid-C and highlights the need for a proper representation of the channel geometry.

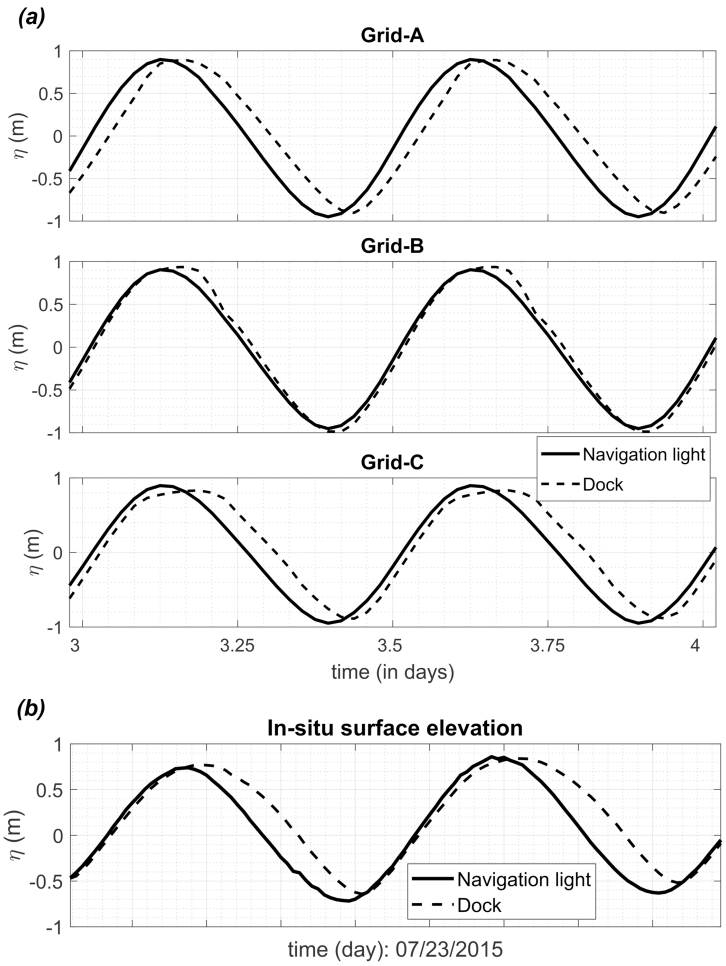

Figure 8: (a) Model water surface elevation comparison between two gauge locations from inlet channel opening and boundary: Navigation light and Dock for a M2 tide (in meters, from NAVD88 vertical reference level). Subplots from the top to bottom shows a sequence of result for different grid conditions, A-C; (b) In-situ water surface elevation comparison during a neap tide condition (in meters, from NAVD88 vertical reference level).

The along-channel surface phase lag for different hypsometry conditions can be also explained in a mechanistic way by using the Saint Venant equations widely used for one-dimensional discharge routing in open channels. According to Brunner and Bonner (2010), for a gradually varying unsteady flow with irregular cross sections, the equations can be written as:

$$\frac{\partial A}{\partial t} + \frac{\partial Q}{\partial x} = 0 \tag{3}$$

$$\frac{\partial Q}{\partial t} + \frac{\partial QU}{\partial x} + gA \left(\frac{\partial z}{\partial x} + S_f \right) = 0 \tag{4}$$

where A is flow area of cross section (bH), Q is discharge (AU), U is x-direction velocity, and $z = z_0 + H$; z_0 is channel elevation and H is the total depth. The friction slope S_f using the Manning equation is

$$S_f = \frac{Q|Q|n^2}{2.208R^{4/3}A^2} \tag{5}$$

where n is Manning's roughness coefficient and R is hydraulic radius, or cross-sectional area A divided by the wetted perimeter.

We developed a 1D unsteady model for the entire Leipsic River (Figure 12a) using the Hydrologic Engineering Center's River Analysis System (version 5.0.7) known as HEC-RAS, that solves equations 3-4. The bathymetric data set HEC-RAS includes 56 cross-sections taken from triangulated irregular network (TIN) data developed from different FVCOM grids, and a stage and flow boundary condition is assigned at the inlet cross-section using FVCOM model surface elevation and volume flux.

For a channel with irregular bathymetry and rapid width contraction and expansion, the along and across-channel properties in equation 3-5 can be separated using still water and tidally varying representations as

$$A(x,t) = A_0(x) \pm A'(x,t) \tag{6}$$

$$b(x,t) = b_0(x) \pm b'(x,t) \tag{7}$$

$$H(x,t) = h_0(x) + \eta(x,t) \tag{8}$$

Here, A_0, b_0 and h_0 represent the channel area, width and depth in a still water condition, and A', b' and η are the tidally varying components.

Among our model grids, Grid-A presents a unique situation where the inaccurate mesh design and the resulting rapid changes in channel width in a short period (due to wetting and drying) controls the phase delay (Figure 9a and 10a). During low tide, the spatial rate of change in channel width $\frac{\partial(b_0-b')}{\partial x}$ is higher than the change in depth $\frac{\partial h_0}{\partial x}$, and dominates the changes in the flow area $\frac{\partial(A_0-A')}{\partial x}$ (Figure 9a). Also, this along-channel rate of change is higher than the time rate of change of the wetted cross-sectional area, that ultimately reduces the channel conveyance and increase the surface phase lag. When tide rises to the level of marsh surface elevation, the along-channel artificial width convergence goes away and model recovers the full flow area. At this point, the time rate of change of the channel width, depth and wetted cross-sectional all become important again along with the spatial change, and contribute to the overall transport. This rapid change in channel cross-section from low model resolution is not trivial to explain using a 1D case and needs subgrid representation of the partially wet elements in 2D calculations. In Grid-B, with higher marsh-channel shoreline resolution shown in Figure 9b and 10b, the spatial and time rate of change in channel width $\frac{\partial b}{\partial x}$ and $\frac{\partial b}{\partial t}$ reduces, and also, as we have kept the same bathymetry, the spatial change in channel depth $\frac{\partial h_0}{\partial x}$ and bottom friction (Equation 5) remain similar to the values from Grid-A. From Figure 12b (top subplot), we can see that the surface phase lag has reduced as tide travels upstream and show a standing wave type condition, similar to the result shown earlier in Figure 8b using FVCOM. In Grid-C, the surveyed bathymetry data has altered the along and across-channel bottom roughness and flow area significantly compared to Grid-B. While, in this case, the rate of change in channel width is similar to Grid-B, the spatial change in channel depth $\frac{\partial h_0}{\partial x}$ (Figure 2b and 9c), change in area $\frac{\partial A}{\partial x}$ and friction (Figure 11c) have become the dominant terms, ultimately reestablishing the phase lag between both gauges again (Figure 12b, bottom subplot).

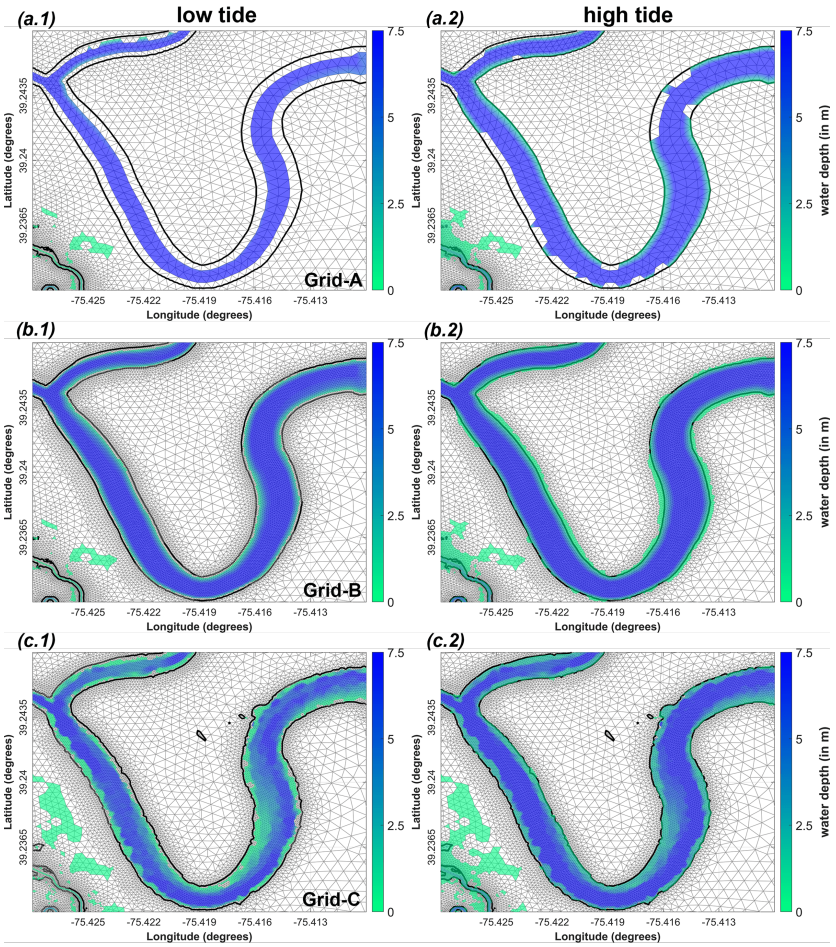

Figure 9: Channel total water depth (surface + bottom elevation, in meters) and width variation during low and high tide, separated into three rows for different grids: (a) lower channel resolution and insufficient channel survey (b) higher channel and berm resolution and bathymetry interpolated from the previous grid (c) higher channel and berm resolution and new dense channel survey data set.

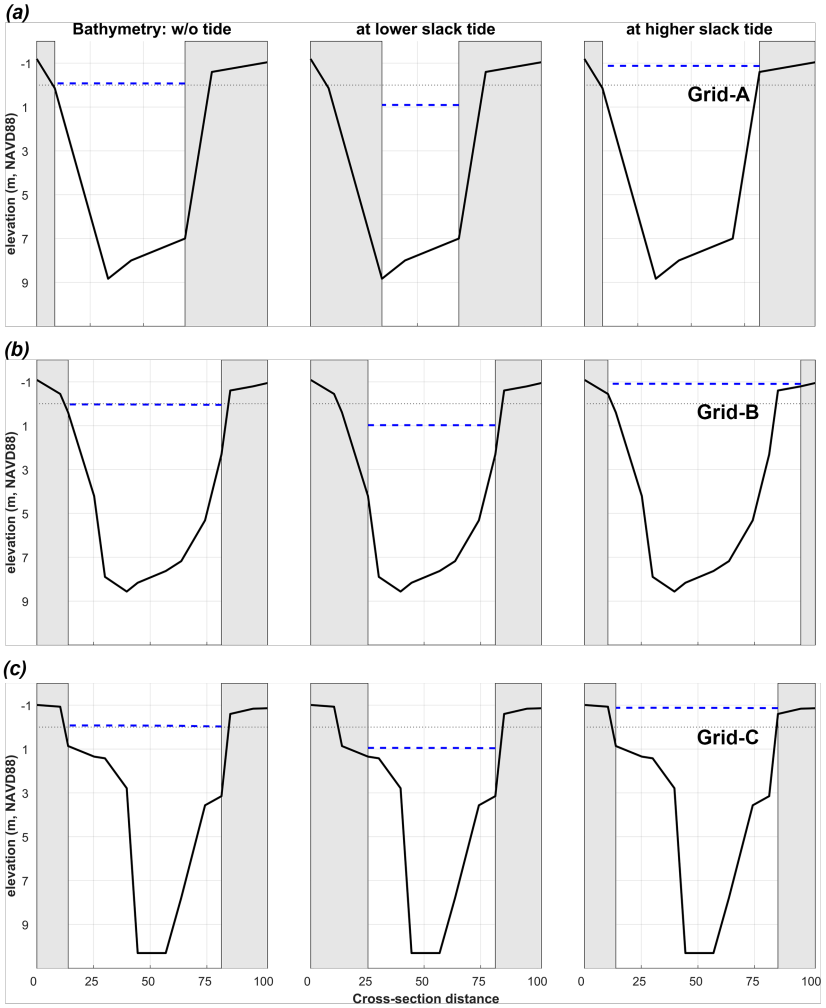

Figure 10: A channel cross-section showing Leipsic River hypsometry for different grid conditions (taken 3 km inward from the inlet mouth). Total water depth and width variation for still water, and during low and high tide are separated into three rows for different grids like Figure 9. Here, gray patch represent dry land seen by model grids during different tidal conditions and the corresponding loss in channel volume. Blue dashed line is the surface elevation and dotted black line is the NAVD88 vertical reference level (in meters).

.

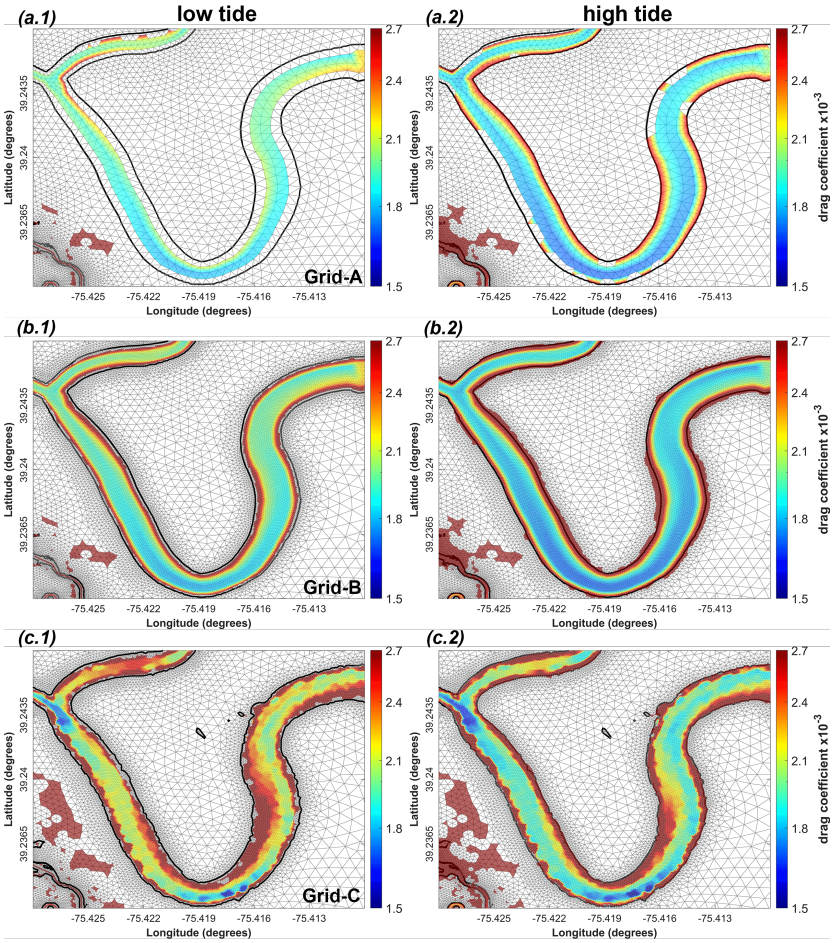

Figure 11: Drag coefficient, C_D during low and high tide estimated using the Manning formula and friction coefficient $n = 0.02$, separated into three rows for different grids: descriptions are similar to Figure 9.

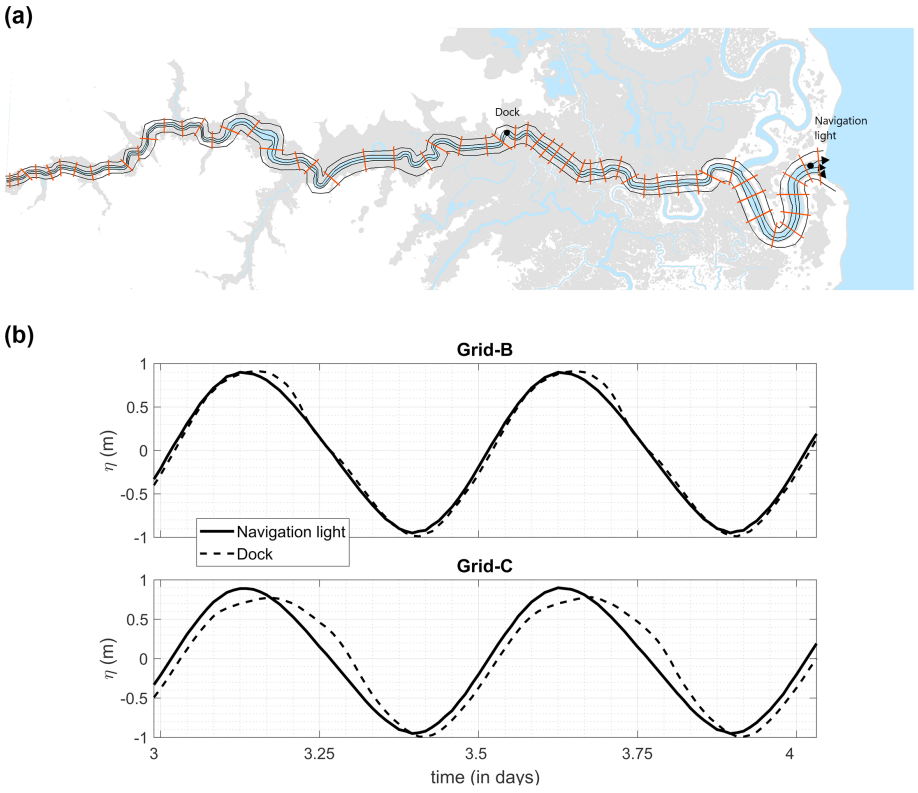

Figure 12: (a) Channel cross-sections used for HEC-RAS 1D unsteady simulations (1D Saint-Venant equations). (b) Water surface elevation comparison between two gauge locations from Leipsic River inlet opening and model boundary: Navigation light and Dock (in meters, from NAVD88 vertical reference level). Subplots from the top to bottom shows a sequence of result for different grid conditions, B-C.

4.3. Channel hypsometry and tidal wave regime

In Figure 13 and 14, with surface elevation, we also have included current & flux information to compare the phase lag between them, which can provide more details on changes to the wave regimes. We applied Matlab's *Hilbert transform* function to both surface and current & flux time series data to generate the analytical signal. Then, using the *angle* and *unwrap* functions, the phase information is extracted. In our cases, we observed that the velocity/flux proceeds surface elevation by varying degrees based on the tidal stage at both inlet and channel boundary. We have estimated flux to take care of the channel geometry and across the channel velocity variation, and identified changes in relative phase $\phi_{\eta u}$ and $\phi_{\eta Q}$ to see the variety in tidal wave types.

For Grid-A, we can see that during flood tide, phase difference both $\phi_{\eta u}$ & $\phi_{\eta Q}$ increases slowly from 60° to almost 90° as the wave travels from inlet mouth to farther upstream (Figure 13a,b). During the flood, the increase in phase difference of $\phi_{\eta u}$ & $\phi_{\eta Q}$ is completely from the artificial channel width variation due to model wetting and drying. It is much more complicated for ebb tide as there is a reflection from the boundary, and it displays characteristics of a standing wave at Dock (u/s location), where $\phi_{\eta u}$ & $\phi_{\eta Q}$ are even slightly higher than 90°. This case has a higher channel depth, corresponding lower bottom friction (Figure 11a), weak convergence, and the phase difference shown at locations close to inlet mouth and boundary are completely from significant width variation during rising and falling tide (Figure 9-11, top row). Throughout the channel, velocity and flux magnitude have dramatically decreased due to the cross-sectional area contraction, topographic dispersion, and flow diversion toward a few other channels. In contrast, the surface elevation magnitude remains almost similar (Figure 13-14 a,b). We have observed good model performance using this Grid-A during both Hurricane Sandy and Joaquin when compared the surface elevation only. Interestingly, it can easily mislead into believing other subsequent model interpretations of velocity and flux estimation. The velocity magnitude is completely out of order compared to the Grid-C, which is validated extensively with field measurements shown in Deb et al. (2022a) and Deb et al. (2018a). With the higher resolution in channels and berm location in Grid-B, the phase difference remains almost unchanged close to 80° during flood shown in Figure 13 and 14 c-d, with a reduced magnitude in

velocity and volume flux. At the beginning of ebb tide, the phase difference between surface and velocity/flux, $\phi_{\eta u}$, and $\phi_{\eta Q}$ shows a complete reflection even at the inlet mouth, and they stay close to 90° which displays characteristics of a standing wave. In this case, the channel caused a minimal damping of the incident and reflected wave due to weak convergence, higher depth, and low roughness even during the low tide (Figure 9-11, middle row). From Figure 13 c-d, we can see that the velocity magnitude is similar to the previous case at the inlet mouth, and almost doubled at the boundary during ebb. Grid-B with improved resolution completely misrepresents the tidal phase speed and surface-velocity/flux phase difference due to incorrect channel bathymetry data, ultimately reflected in our comparisons for Hurricane Sandy and Joaquin (Figure 4-5). Finally, in Grid-C with surveyed bathymetry, both $\phi_{\eta u}$ and $\phi_{\eta Q}$ show a different behavior than Grid-A and Grid-B, and the surface-velocity/flux phase lag seems to decrease with rising tide and wave regime represents a progressive type (Figure 13-14 e-f). During ebb, the cross-section averaged depth decreases, bottom friction becomes dominant and slows the incident wave propagation further. Figure 13 and 14 (f) shows the increase in phase lag between surface and velocity/flux at the boundary due to reflection, and it reaches close to 90°. This case illustrates the time-dependent relationship between changes in channel width and depth and tidal phase speed, and how it can change between progressive and standing wave during high and low tide. Grid-C provided the most reliable performance considering both surface elevation and velocity comparisons, and the velocity comparisons are shown in Deb et al. (2022a), where Grid-C is used extensively.

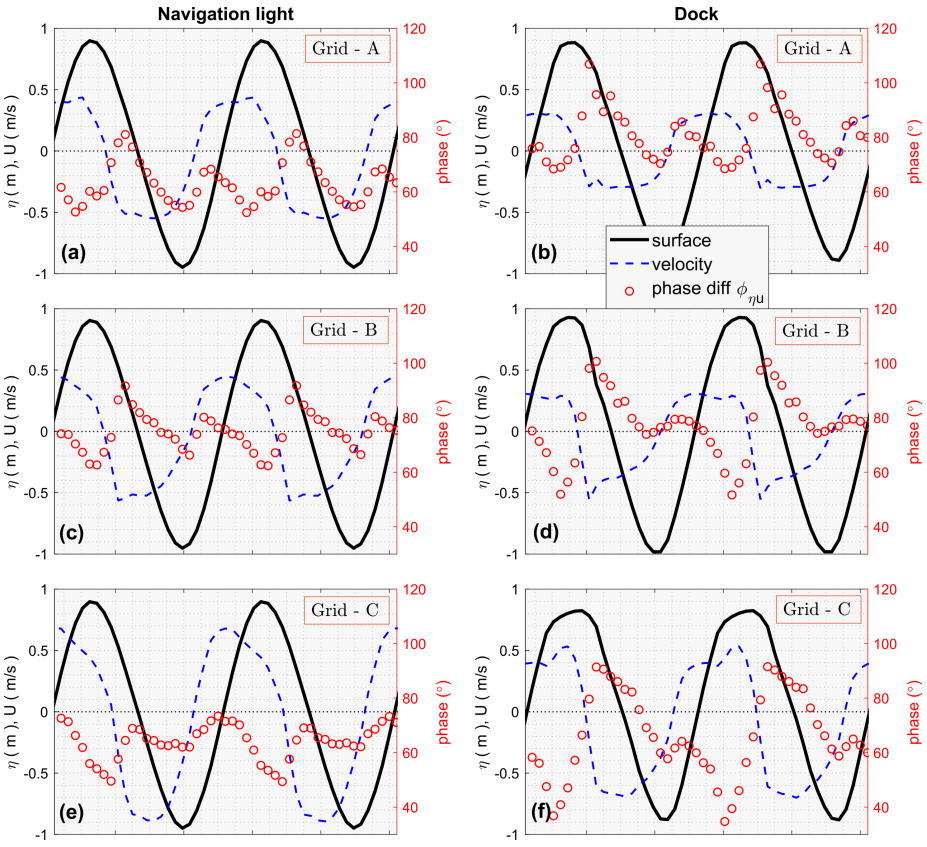

Figure 13: Phase difference (in degrees) between model water surface (in meters) and mid-channel velocity (in m/s) from two gauge locations at inlet channel opening and boundary: Navigation light and Dock respectively (separated into 2 columns). Subplots from the top to bottom (a,c,e & b,d,f) shows a sequence of result for different grid conditions, A-C.

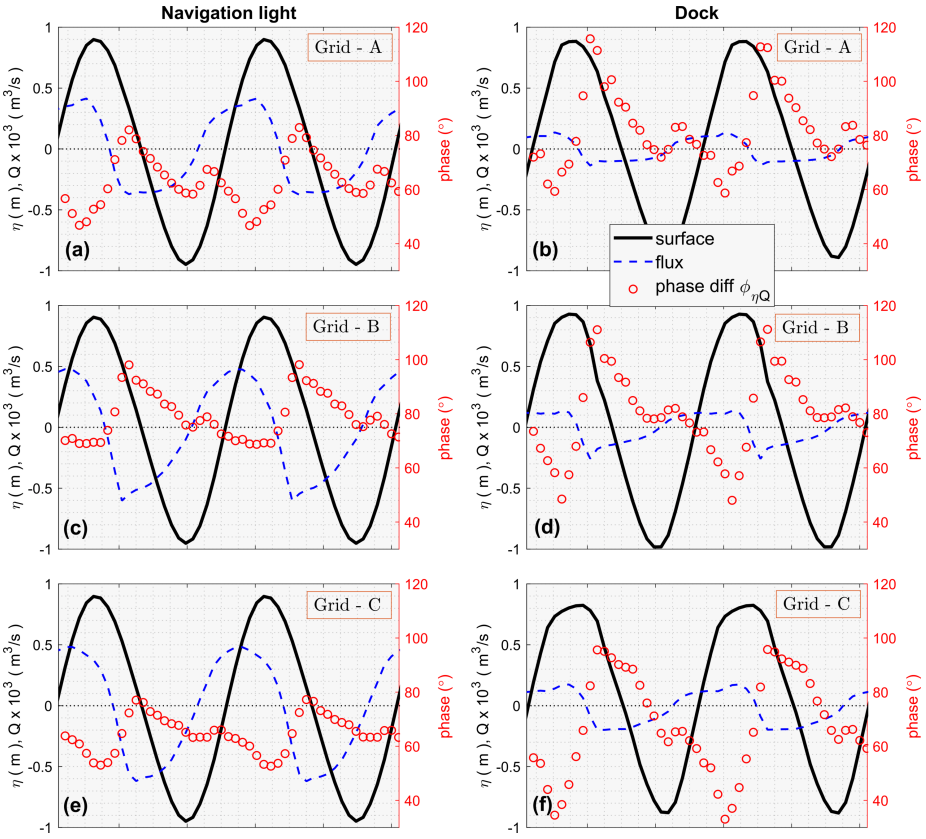

Figure 14: Phase difference (in degrees) between model water surface (in meters) and channel volume flux (in m^3/s) from two gauge locations at inlet channel opening and boundary: Navigation light and Dock respectively (separated into 2 columns). Subplots from the top to bottom (a,c,e & b,d,f) shows a sequence of result for different grid conditions, A-C.

5. Concluding remarks and future works

We have presented an overview of how the accurate representation of wetland channel hypsometry can significantly improve the overall hydrodynamic modeling skill and reliability. Mainly, two essential variables, model grid resolution around the marsh-channel shoreline and channel bathymetry, are observed to define the model calculations for major physical processes. Inaccurate channel geometry from lower density survey and model resolution can provide good agreement with in-situ surface elevation data; however, it completely misses the tidal velocity and phase. This better surface elevation and phase prediction are observed to result from the artificial channel convergence due to model low resolution around marsh edges. An increase in the grid resolution helped to identify the wet/dry boundary better, but has shown a dramatic decrease in the model skill because of the existing low-density channel survey data that misrepresents the channel hypsometry and bottom friction. Finally, with a higher density channel survey inside the wetland, the model calculation of surface elevation has improved, along with the velocity magnitude and phase. An accurate estimate of the tidal velocity and relative phase difference between current and surface is essential for determining asymmetry, wave regime, and the residual flow. Ultimately, it contributes toward having a reliable hydrodynamic model, and further sediment transport calculations and net budget of the entire wetland system.

This study has shown the role of channel hypsometry only, and kept the influence of marsh topography separate for a different study. The marsh topography is an essential variable in controlling the platform wetting and drying, and the estuary width variation. However, due to the modeling limitation: artificial ponding in isolated marsh depressions, we have shown the importance of wetland channels in controlling the tidal hydrodynamics. More details on the artificial ponding and the necessary fixes are given in Deb et al. (2022b). Lastly, another important limitation of the proposed modeling procedure is an increase in computational time ($\sim$ 20% increase in model completion time for the finer grid), which adds a computational burden for longer-term simulations. While several subgrid models are available to reduce the computational expense for longer-term wetland studies, it is still challenging to adequately address the sharp

marsh-channel edge and small-scale bathymetric features in the subgrid bed adjustments.

Acknowledgments: This work has been supported by the National Fish and Wildlife Foundation and the US Department of the Interior under Grant No. 43752 to the University of Delaware, and by Delaware Sea Grant program award R/HCE-22 and RRCE-12. The authors acknowledge Conor McDowell and Christopher Sommerfield (deceased) for providing the channel bathymetry data sets. Andre Rodrigues and Tobias Kukulka provided the large scale ROMS simulation outputs. The findings and conclusions in this article are those of the author(s) and do not necessarily represent the views of the National Fish and Wildlife Foundation. This research was also supported in part through the use of Information Technologies (IT) resources at the University of Delaware, specifically the high-performance computing resources.

References

Aquaveo, L., 2016. Surface-water modeling system, version 12.1. Reference manual & tutorials, Provo, UT .

Aubrey, D.G., Speer, P.E., 1985. A Study of Non-linear Tidal Propagation in shallow inlet / estuarine systems Part I : Observations. Estuarine, Coastal and Shelf Science 21, 185–205. doi:doi:10.1016/0272-7714(85)90096-4.

Bomers, A., Schielen, R.M., Hulscher, S.J., 2019. The influence of grid shape and grid size on hydraulic river modelling performance. Environmental Fluid Mechanics URL: https://doi.org/10.1007/s10652-019-09670-4, doi:10.1007/s10652-019-09670-4.

Boon, J.D., Byrne, R.J., 1981. On basin hyposmetry and the morphodynamic response of coastal inlet systems. Marine Geology 40, 27–48. doi:10.1016/0025-3227(81)90041-4.

Brunner, G., Bonner, V., 2010. HEC River Analysis System (HEC-RAS) Version 4.1 January 2010 , 411URL: http://oai.dtic.mil/oai/oai?verb=getRecord{&}metadataPrefix=html{&}identifier=ADA289522.

Chen, C., Qi, J., Li, C., Beardsley, R.C., Lin, H., Walker, R., Gates, K., 2008. Complexity of the flooding/drying process in an estuarine tidal-creek salt-marsh system: An application of FVCOM. Journal of Geophysical Research: Oceans 113. doi:10.1029/2007JC004328.

Chen, J.L., Shi, F., Hsu, T.J., Kirby, J.T., 2014. NearCOM TVD A quasi-3D nearshore circulation and sediment transport model. Coastal Engineering 91, 200–212.

Deb, M., Abdolali, A., Kirby, J.T., Shi, F., 2018a. Hydrodynamics, sediment transport and wind waves in an eroding salt marsh environment. Bombay Hook National Wildlife Refuge, Delaware. Research Report CACR-18-04. Center for Applied Coastal Research, Department of Civil and Environmental Engineering, University of Delaware. Newark, DE.

Deb, M., Abdolali, A., Kirby, J.T., Shi, F., Guiteras, S., McDowell, C., 2022a. Sensitivity of tidal hydrodynamics to varying bathymetric configurations in a multi-inlet rapidly eroding salt marsh system: A numerical study. Earth Surface Processes and Landforms n/a.

Deb, M., Abdolali, A., McDowell, C., Kirby, J.T., Sommerfield, C.K., Shi, F., 2018b. Hydrodynamic, survey and sediment data collection. Bombay Hook National Wildlife Refuge, Delaware. Research Report CACR-18-03. Center for Applied Coastal Research, Department of Civil and Environmental Engineering, University of Delaware. Newark, DE.

Deb, M., Kirby, J.T., Shi, F., Abdolali, A., 2022b. A surface porosity approach for eliminating artificial ponding in coastal salt marsh simulations. JGR: Earth Surface submitted.

Defina, A., 2000. Two-dimensional shallow flow equations for partially dry areas. Water Resources Research 36, 3251–3264. doi:10.1029/2000WR900167.

Dierssen, H.M., Theberge, A.E., 2014. Bathymetry: Assessing methods. Encyclopedia of Ocean Sciences .

Dietrich, J.C., Tanaka, S., Westerink, J.J., Dawson, C., Luettich, R., Zijlema, M., Holthuijsen, L.H., Smith, J., Westerink, L., Westerink, H., 2012. Performance of the unstructured-mesh, SWAN+ ADCIRC model in computing hurricane waves and surge. Journal of Scientific Computing 52, 468–497.

Dohner, S., Trembanis, A., Miller, D., 2016. A tale of three storms: Morphologic response of Broadkill Beach, Delaware, following Superstorm Sandy, Hurricane Joaquin, and Winter Storm Jonas. Shore & Beach 84, 3.

Friedrichs, C.T., 2010. Barotropic tides in channelized estuaries. Contemporary Issues in Estuarine Physics , 27–61doi:10.1017/CBO9780511676567.004.

Friedrichs, C.T., Aubrey, D.G., 1988. Nonlinear tidal distortion in shallow well-mixed estuaries. Estuarine, Coastal and Shelf Science 27, 521–545. doi:10.1016/0272-7714(90)90054-U.

Horritt, M., Bates, P., 2001. Predicting floodplain inundation: raster-based modelling versus the finite-element approach. Hydrological processes 15, 825–842.

Horritt, M., Bates, P., Mattinson, M., 2006. Effects of mesh resolution and topographic representation in 2d finite volume models of shallow water fluvial flow. Journal of Hydrology 329, 306–314.

Hunt, J.N., 1964. Tidal Oscillations in Estuaries. Geophysical Journal International 8, 440–455.

Jay, D.A., 1991. Green's law revisited: Tidal long-wave propagation in channels with strong topography. Journal of Geophysical Research 96, 20585. doi:10.1029/91JC01633.

Kukulka, T., Jenkins III, R.L., Kirby, J.T., Shi, F., Scarborough, R.W., 2017. Surface wave dynamics in Delaware Bay and its adjacent coastal shelf. Journal of Geophysical Research: Oceans 122, 8683–8706. doi:10.1002/2017JC013370.

Lesser, G.R., Roelvink, J.v., Van Kester, J., Stelling, G., 2004. Development and validation of a three-dimensional morphological model. Coastal engineering 51, 883–915.

Li, Z., Hodges, B.R., 2020. On modeling subgrid-scale macro-structures in narrow twisted channels. Advances in Water Resources 135, 103465. URL: https://doi.org/10.1016/j.advwatres.2019.103465, doi:10.1016/j.advwatres.2019.103465.

Luettich Jr, R.A., Westerink, J.J., Scheffner, N.W., 1992. ADCIRC: An Advanced Three-Dimensional Circulation Model for Shelves, Coasts, and Estuaries. Report 1. Theory and Methodology of ADCIRC-2DDI and ADCIRC-3DL. Technical Report. Coastal engineering research center Vicksburg MS.

Nidzieko, N.J., 2010. Tidal asymmetry in estuaries with mixed semidiurnal/diurnal tides. Journal of Geophysical Research: Oceans 115, 1–13. doi:10.1029/2009JC005864.

Parker, B.B., 1984. Friction Effects on the Tidal Dynamics of a Shallow Estuary. Ph.D. thesis.

Pawlowicz, R., Beardsley, B., Lentz, S., 2002. Classical tidal harmonic analysis including error estimates in MATLAB using T_TIDE. Computers & Geosciences 28, 929–937. doi:10.1016/S0098-3004(02)00013-4.

Ralston, D.K., Geyer, W.R., Warner, J.C., 2012. Bathymetric controls on sediment transport in the Hudson River estuary: Lateral asymmetry and frontal trapping. Journal of Geophysical Research: Oceans 117, 1–21. doi:10.1029/2012JC008124.

Sanders, B.F., Schubert, J.E., Gallegos, H.A., 2008. Integral formulation of shallow-water equations with anisotropic porosity for urban flood modeling. Journal of Hydrology 362, 19–38. URL: http://dx.doi.org/10.1016/j.jhydrol.2008.08.009, doi:10.1016/j.jhydrol.2008.08.009.

Schmid, K.A., Hadley, B.C., Wijekoon, N., 2011. Vertical accuracy and use of topographic lidar data in coastal marshes. Journal of Coastal Research 27, 116–132. doi:10.2112/JCOASTRES-D-10-00188.1.

Stammerman, R., 2013. Hydrodynamics and sediment transport studies in tidal marshes of the Delaware Bay using high resolution numerical models. Ph.D. thesis. Drexel University.

Sullivan, K., Uccellini, L., 2013. Service assessment: Hurricane/post-tropical cyclone sandy, october 22–29, 2012. US Department of Commerce NOAA and NWS, Silver Spring, Maryland 66.

Symonds, A.M., Vijverberg, T., Post, S., van der Spek, B.J., Henrotte, J., Sokolewicz, M., 2017. Comparison between MIKE 21 FM, Delft3D and Delft3D FM flow models of Western Port Bay, Australia. Coastal Engineering Proceedings 1, 11.

Temmerman, S., Bouma, T.J., Govers, G., Wang, Z.B., De Vries, M.B., Herman, P.M.J., 2005. Impact of vegetation on flow routing and sedimentation patterns: Three-dimensional modeling for a tidal marsh. Journal of Geophysical Research: Earth Surface 110. URL: https://agupubs.onlinelibrary.wiley.com/doi/abs/10.1029/2005JF000301, doi:https://doi.org/10.1029/2005JF000301, arXiv:https://agupubs.onlinelibrary.wiley.com/doi/pdf/10.1029/2005JF000301.

Temmerman, S., De Vries, M.B., Bouma, T.J., 2012. Coastal marsh die-off and reduced attenuation of coastal floods: A model analysis. Global and Planetary Change 92-93, 267–274. URL: https://www.sciencedirect.com/science/article/pii/S0921818112001130, doi:https://doi.org/10.1016/j.gloplacha.2012.06.001.

Van Rijn, L., et al., 2010. Tidal phenomena in the scheldt estuary .

Volp, N.D., van Prooijen, B.C., Stelling, G.S., 2013. A finite volume approach for shallow water flow accounting for high-resolution bathymetry and roughness data. Water Resources Research 49, 4126–4135. URL: https://agupubs.onlinelibrary.wiley.com/doi/abs/10.1002/wrcr.20324, doi:https://doi.org/10.1002/wrcr.20324, arXiv:https://agupubs.onlinelibrary.wiley.com/doi/pdf/10.1002/wrcr.20324.

Willmott, C.J., 1981. On the validation of models. Physical Geography 2, 184–194. doi:10.1080/02723646.1981.10642213.

Wu, G., Shi, F., Kirby, J.T., Mieras, R., Liang, B., Li, H., Shi, J., 2016. A pre-storage, subgrid model for simulating flooding and draining processes in salt marshes. Coastal Engineering 108, 65–78. URL: http://dx.doi.org/10.1016/j.coastaleng.2015.11.008, doi:10.1016/j.coastaleng.2015.11.008.

Yu, D., Lane, S.N., 2006. Urban fluvial flood modelling using a two-dimensional diffusion-wave treatment, part 1: Mesh resolution effects. Hydrological Processes 20, 1541–1565. doi:10.1002/hyp.5935.